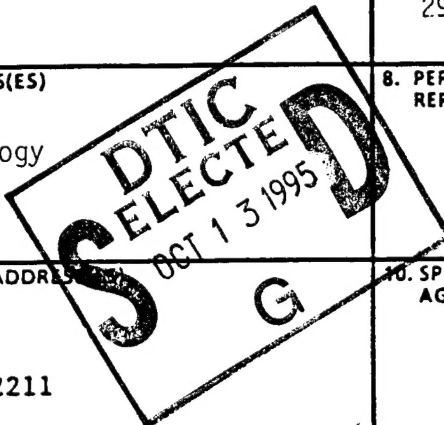


REPORT DOCUMENTATION PAGE			Form Approved OMB No. 0704-0188	
<small>Public reporting burden for this collection of information is estimated to average 1 hour per response, including the time for reviewing instructions, searching existing data sources, gathering and maintaining the data needed, and completing and reviewing the collection of information. Send comments regarding this burden estimate or any other aspect of this collection of information, including suggestions for reducing this burden, to Washington Headquarters Services, Directorate for Information Operations and Reports, 1215 Jefferson Davis Highway, Suite 1204, Arlington, VA 22202-4302, and to the Office of Management and Budget, Paperwork Reduction Project (0704-0188), Washington, DC 20503.</small>				
1. AGENCY USE ONLY (Leave blank)	2. REPORT DATE 8/9/95	3. REPORT TYPE AND DATES COVERED Final 6/1/92 - 5/31/95		
4. TITLE AND SUBTITLE Far-Infrared (THz) Lasers Using Multiple Quantum Wells		5. FUNDING NUMBERS DAAL03-92-G-0251		
6. AUTHOR(S) Prof. Qing Hu		29578-PH		
7. PERFORMING ORGANIZATION NAME(S) AND ADDRESS(ES) Research Laboratory of Electronics Massachusetts Institute of Technology 77 Massachusetts Avenue Cambridge, MA 02139-4307		8. PERFORMING ORGANIZATION REPORT NUMBER		
9. SPONSORING/MONITORING AGENCY NAME(S) AND ADDRESS(ES) U. S. Army Research Office P. O. Box 12211 Research Triangle Park, NC 27709-2211		10. SPONSORING/MONITORING AGENCY REPORT NUMBER		
11. SUPPLEMENTARY NOTES The view, opinions and/or findings contained in this report are those of the author(s) and should not be construed as an official Department of the Army position, policy, or decision, unless so designated by other documentation.				
11a. DISTRIBUTION/AVAILABILITY STATEMENT Approved for public release; distribution unlimited.			12b. DISTRIBUTION CODE	
13. ABSTRACT (Maximum 200 words) This project is to develop THz solid-state lasers using multiple-quantum-well (MQW) structures. Based on work in our group and other groups outside MIT in the last few years, we have focused our effort on using double quantum-well (DQW) structures to achieve this goal. In essence, a DQW device is a voltage-tunable two-level system, as far as the interwell intersubband transition is concerned. Thus, compared to intrawell intersubband-transition devices that have been proposed and studied, the DQW device has a greater tolerance for design and fabrication errors. This is a major advantage over Bloch oscillators using superlattices, in which the unavoidable formation of high-field domains will lead to a significant misalignment of energy levels through the superlattice. Since the relative energy difference between the lowest two levels in a DQW structure is voltage tunable, the same structure can also be used for far-infrared detection as well as generation, if the initial state lies below the final state. In the current three-year project, we have explored the potential of far-infrared generation and detection using DQWs. We have performed an extensive theoretical study on the radiation properties of DQW structures, such as gain, loss, and efficiency. We have also performed an extensive study using magnetotunneling spectroscopy to accurately determine the relative subband levels in the DQW structures.				
14. SUBJECT TERMS DTIC QUALITY INSPECTED 5			15. NUMBER OF PAGES	
			16. PRICE CODE	
17. SECURITY CLASSIFICATION OF REPORT UNCLASSIFIED	18. SECURITY CLASSIFICATION UNCLASSIFIED	19. SECURITY CLASSIFICATION OF ABSTRACT UNCLASSIFIED	20. LIMITATION OF ABSTRACT UL	



19951011 108

FAR-INFRARED LASERS

Final Report

Table of Contents

Accession For	
NTIS CRA&I	<input checked="" type="checkbox"/>
DTIC TAB	<input type="checkbox"/>
Unannounced	<input type="checkbox"/>
Justification _____	
By _____	
Distribution /	
Availability Codes	
Dist	Avail and/or Special
A-1	

	Page
I. Abstract	2
II. Introduction	3
III. Gain, loss, and lasing threshold for DQW structures	
III.1 Radiation properties and gain of a single DQW device	4
III.2 Scattering and lasing threshold current density	11
III.3 Magnetic suppression of nonradiative intersubband scattering	14
III.4 Magneto-tunneling spectroscopy	16
III.5 List of participating scientific personnel	20

I. Abstract

This project is to develop THz solid-state lasers using multiple-quantum-well (MQW) structures. Based on work in our group and other groups outside MIT in the last few years, we have focused our effort on using double quantum-well (DQW) structures to achieve the goal. In essence, a DQW device is a voltage-tunable two-level system, as far as the interwell intersubband transition is concerned. Thus, compared to intrawell intersubband-transition devices that have been proposed and studied, the DQW device has a greater tolerance for design and fabrication errors. This is a major advantage over Bloch oscillators using superlattices, in which the unavoidable formation of high-field domains will lead to a significant misalignment of energy levels through the superlattice. Since the relative energy difference between the lowest two levels in a DQW structure is voltage tunable, the same structure can also be used for far-infrared detection as well as generation, if the initial state lies below the final state. In the current three-year project, we have explored the potential of far-infrared generation and detection using DQWs. We have performed an extensive theoretical study on the radiation properties of DQW structures, such as gain, loss, and efficiency. We have also performed an extensive study using magnetotunneling spectroscopy to accurately determine the relative subband levels in the DQW structures.

II. INTRODUCTION

Far-infrared or THz frequencies are among the most underdeveloped electromagnetic spectra, even though their potential application in spectroscopy, astrophysics, plasma diagnostics, remote sensing and imaging, and space-based radar and communications are obviously great. This underdevelopment is because the far-infrared or THz frequency range falls between two other frequency ranges in which conventional semiconductor devices have been successfully employed. One is the microwave and millimeter-wave frequency range, and the other is the near-infrared and optical frequency range. Semiconductor devices that utilize the classical diffusive transport of electrons, such as diodes and transistors, have a high frequency limitation of several hundred GHz. This is limited by electron mobility and the smallest feature size that can be fabricated. Semiconductor devices based on quantum mechanical interband transitions, however, are limited to frequencies higher than those corresponding to the semiconductor energy gap, which is higher than 10 THz for most bulk semiconductors. Therefore, a large gap exists from 100 GHz to 10 THz, in which very few solid-state devices are available.

Semiconductor quantum wells are human-made quantum mechanical systems in which the energy levels can be chosen by changing the dimensions of the quantum wells. Long-wavelength photoelectric devices that utilize the intersubband transitions, such as far-infrared lasers, have been proposed.¹⁻⁶ Significant progress was made recently toward this goal. Large oscillator strengths of intersubband transitions have been observed in far-infrared absorption spectroscopy experiments.^{7,8} An intersubband spontaneous emission with a power level of $\sim 10^{-7}$ W has been observed.^{9,10} Despite the encouraging preliminary results, far-infrared lasing has not yet been achieved, even though unipolar lasers based on intersubband transitions have been developed at near-infrared frequencies ($\lambda \approx 4 \mu\text{m}$).¹¹ Two main obstacles are especially difficult to overcome at far-infrared frequencies. The first one is the extremely unfavorable ratio of the radiative relaxation rate $1/\tau_{\text{spon}}$ over that of the nonradiative rate $1/\tau_{\text{ac}} + 1/\tau_{\text{LO}} + 1/\tau_{\text{e-e}}$, which is due to acoustic-phonon, LO-phonon, and electron-electron scattering. Specifically, for intersubband transitions within a single quantum well (intrawell) at THz frequencies, $\tau_{\text{spon}} \sim 1 \mu\text{s}$, $\tau_{\text{ac}} \sim 100 \text{ ps}$, $\tau_{\text{LO}} < 1 \text{ ps}$, and $\tau_{\text{e-e}} \sim 1 \text{ ps}$ for a carrier density of $10^{12}/\text{cm}^2$. For interwell transitions, these rates will be reduced by the tunneling probability T through the middle barrier; except e-e scattering rate is reduced by T^2 , since two electrons must traverse the barrier. The second obstacle is the mode confinement. The dielectric waveguide technology that was successfully used at near-infrared frequencies has a low loss of less than 10 cm^{-1} . While the plasma confinement⁵ used at far-infrared frequencies has a heavy loss of several hundred cm^{-1} , due to the low mobility associated with heavy doping in the plasma region.

In the current project, we have explored to use many identical DQW structures that are connected in series in order to overcome these two difficulties. By using such structures, the required inverted population density can be spread out to many DQW modules in order to keep the two-dimensional density low (for example, $1.5 \times 10^{11}/\text{cm}^2$) in each module. In this way, the difference between the Fermi energy and the lower subband level will be below $\hbar\omega_{\text{LO}}$, so that the LO-phonon scattering will not occur. Furthermore, the electron-electron scattering will be reduced at low carrier densities. We have also applied a longitudinal magnetic field (along the current) to further suppress the nonradiative relaxation processes in order to improve the radiation efficiency.^{12,13} The active region's greater thickness of many DQW structures will enhance the mode-confinement factor, thus reducing relative loss due to the plasma walls.

III. Gain, loss, and lasing threshold for DQW structures

III.1 Radiation properties and gain of a single DQW device¹⁴

The schematic of a single DQW structure is shown in Fig. 1(a). The conduction band profile, subband structures, and carrier densities are calculated self-consistently from Schrödinger and Poisson equations, after typical five iterations. Fig. 1(b) shows the transmission coefficient through such a structure, whose peaks correspond to the subband levels in Fig. 1(a). Clearly, the intersubband energy difference $E_2 - E_1$ (corresponding to the radiation frequency) can be tuned by a bias voltage between the emitter and collector. The most important parameter that determines the radiation properties (due to the $1 \rightarrow 2$ intersubband transition) of this DQW structure is the dipole moment $\langle 1|z|2 \rangle$, or equivalently, the oscillator strength f_{12} , which is the ratio of the quantum mechanical radiative decay rate over that of a classical Hertzian dipole at the same frequency.

Before proceeding with numerical calculations, it is instructive to gain insight into the functional relationship of the oscillator strength and the energy splitting for a given anticrossing gap Δ_0 (which is the minimum value of $|E_2 - E_1|$). This is done by analytically solving the problem using a coupled two-level model. Express the stationary eigenstates $|1\rangle$ and $|2\rangle$ in terms of superpositions of states localized in the left and right well, $|L\rangle$ and $|R\rangle$,

$$|1\rangle = c_L^1 |L\rangle + c_R^1 |R\rangle,$$

and

$$|2\rangle = c_L^2 |L\rangle + c_R^2 |R\rangle.$$

Here, $|c_{L,R}^{1,2}|^2$ is the probability of finding a particle in well L (or R) for the eigenstate $|1\rangle$ (or $|2\rangle$). The resulting Heisenberg equation becomes,

$$\begin{bmatrix} E_0 - E_{1,2} - eV/2 & -\Delta_0/2 \\ \Delta_0/2 & E_0 - E_{1,2} + eV/2 \end{bmatrix} \begin{bmatrix} c_L^{1,2} \\ c_R^{1,2} \end{bmatrix} = 0. \quad (1)$$

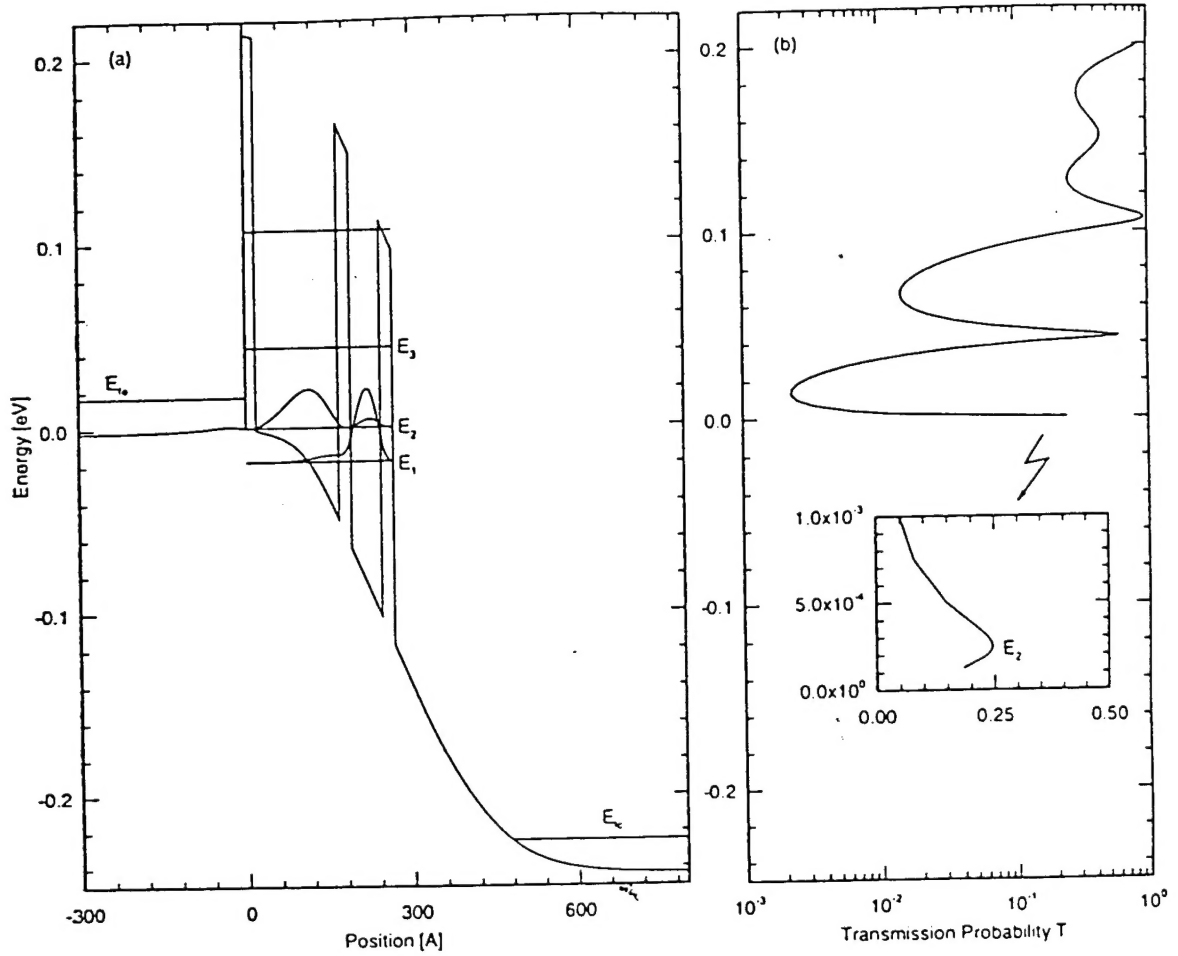
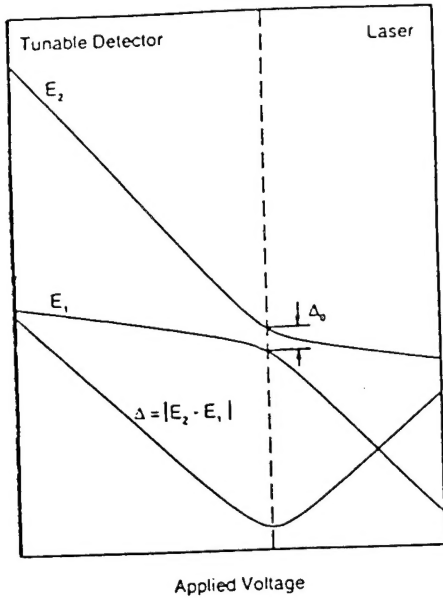


Figure 1. (a) Conduction band profile and the square of wavefunctions at a bias voltage of 240 mV for a typical DQW structure. The wider emitter well (on the left) is to ensure that a large carrier density can be achieved at a desired intersubband spacing $E_2 - E_1$. (b) Transmission coefficient $T(E)$ as a function of the electron incident energy. The peak positions in $T(E)$ correspond to the subband levels in (a). The resonance widths in $T(E)$ determine the escape lifetimes.

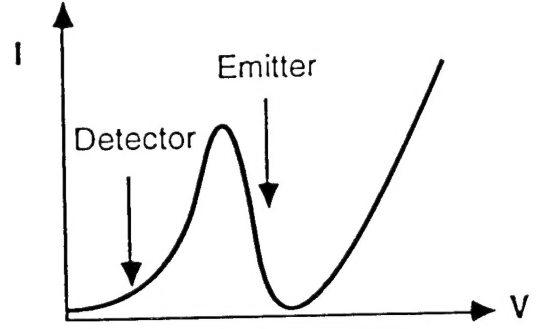
Here, E_0 is the eigenenergy in well $|L\rangle$ when it is isolated from the well $|R\rangle$, V is the potential difference between the two wells at the well centers. The solution of Eq. (1) is

$$E_{2,1} = E_0 \pm \sqrt{(\Delta_0/2)^2 + (eV/2)^2}, \quad (2)$$

and the field-induced energy splitting $\Delta = |E_2 - E_1| = \sqrt{(\Delta_0)^2 + (eV)^2}$. Δ as a function of the bias voltage V is shown in Fig. 2. The energy splitting takes the minimum value Δ_0 at the anticrossing point, above which the energy of the state that is mainly localized in the left well becomes higher than that of



(a)



(b)

Figure 2. (a) Energy level diagram as a function of applied voltage, which exhibits an anti-crossing with a gap Δ_0 . At low voltages the device can be used as a tunable detector, as indicated in (b), and beyond the anti-crossing it functions as a field-tunable emitter.

the state that is mainly localized in the right well, shown in Fig. 1(a). Since the state mainly localized in the left well couples strongly to the emitter (which always has a higher Fermi energy than the collector), and is therefore the initial state that is filled with electrons, Fig. 2 indicates that the relative energy difference between the initial and final states (not only the amplitude but also the sign) can be tuned by the bias voltage. Consequently, the same DQW structure can be used as both a detector and an emitter. As a detector, the initial state lies below the final one; while as an emitter, the initial state lies above the final one.

Semiquantitatively, the coupling strength of the DQW to the emitter and collector reservoirs can be estimated from the probability of finding a particle in the left (emitter) and right (collector) well, and they are,

$$|c_L^{1,2}|^2 = \frac{1}{1 + e^{\pm\theta}} ,$$

and

$$|c_R^{1,2}|^2 = 1 - |c_L^{1,2}|^2 ,$$

where θ is defined by

$$\sinh(\theta/2) = eV/\Delta_0 .$$

These probabilities are plotted in Fig. 3. At the anticrossing gap $\Delta = \Delta_0$, $|c_L^{1,2}|^2 = |c_R^{1,2}|^2 = 0.5$, the wave functions for states $|1\rangle$ and $|2\rangle$ are completely delocalized. The two wells have the strongest coupling at this point. As Δ deviates from the anticrossing gap Δ_0 , however, the probability deviates from 0.5 and the wave functions are localized in either the left or the right well. This is a field-induced

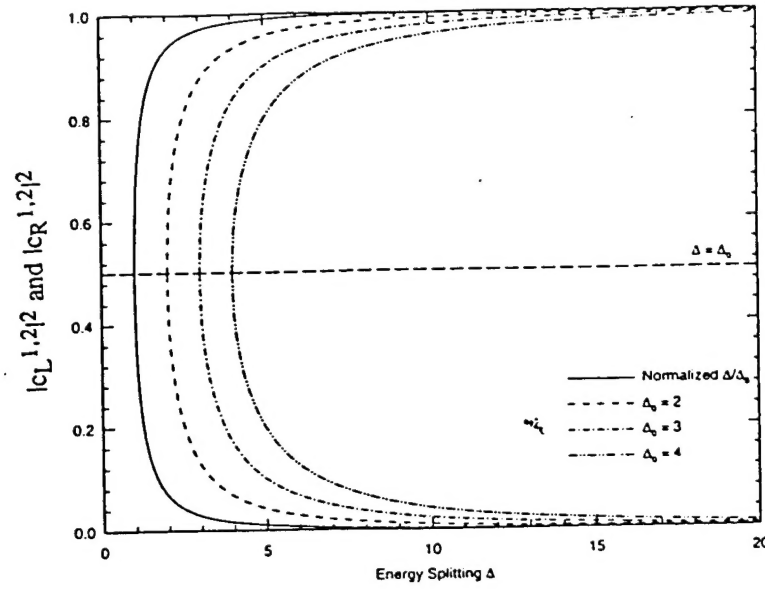


Figure 3. Probabilities $|c|^2$ as functions of energy splitting Δ and anti-crossing gap Δ_0 .

Wannier-Stark localization. As shown in Fig. 3, the probability $|c|^2$ becomes approximately 90% (or 10%) at a normalized $\Delta/\Delta_0 = 2$. Thus, the decoupling of the two wells is a rather rapid function of the energy-splitting Δ/Δ_0 . This decoupling has the benefit of making selective population and depopulation easier (since the upper-level state is mainly coupled to the emitter while the lower-level state is to the collector). However, it also has the adverse effect of reducing the dipole moment (or the oscillator strength) of the $|1\rangle \rightarrow |2\rangle$ intersubband transition. Therefore, we usually consider the case of $\Delta/\Delta_0 \approx 2-4$ in our design analysis for the best trade-off between selective injection and a large oscillator strength.

Analytically, the dipole moment can be shown to be

$$|\langle 1 | z | 2 \rangle|^2 = \frac{W^2 \Delta_0^2}{4 \Delta^2}, \quad (3)$$

where W is the distance between the centers of the two wells. Consequently, the oscillator strength becomes,

$$\begin{aligned} f_{12} &= \frac{2m^*}{\hbar^2} |E_2 - E_1| |\langle 1 | z | 2 \rangle|^2 \\ &= \frac{2m^* W^2}{\hbar^2} \frac{\Delta_0^2}{4 \Delta^2}. \end{aligned} \quad (4)$$

Fig. 4 shows the oscillator strengths as functions of the emission frequency $\Delta = |E_2 - E_1|$ (1 THz = 4 meV), with the anti-crossing gap Δ_0 as a parameter. Fig. 4 also shows the required barrier width and the Al concentration for a chosen value of Δ_0 for GaAs/AlGaAs quantum wells through the relation,^{15,16}

$$\Delta_0 = \frac{\hbar^2}{m^*} \frac{2\pi}{d\lambda} e^{-2\pi d/\lambda},$$

where

$$\lambda = h/\sqrt{2m^*E_B},$$

d and E_B are the barrier width and height, respectively.

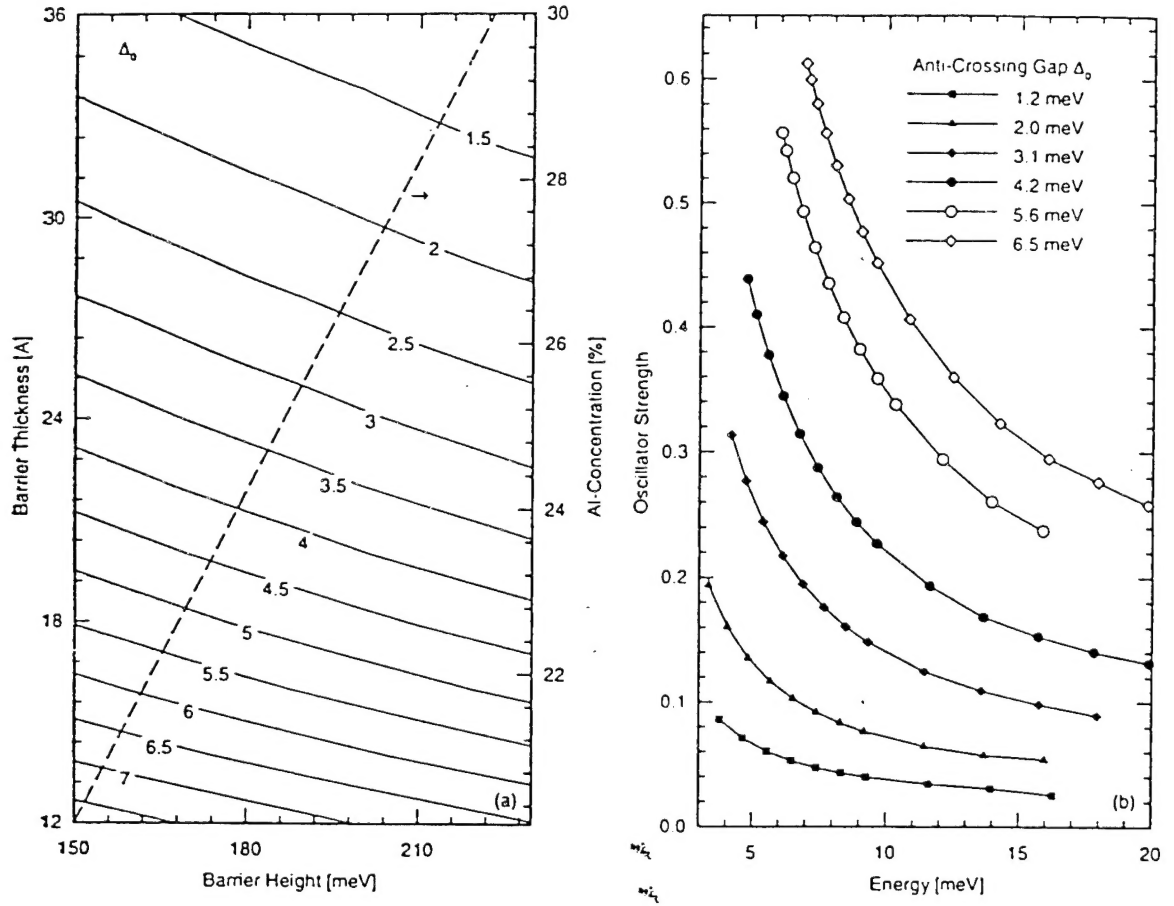


Figure 4. (a) Contour plot of the anticrossing gap Δ_0 as a function of the barrier height and width. The right axis presents the Al concentration as a function of the barrier height in the GaAs/AlGaAs material systems. (b) The oscillation strength as a function of emitted photon energy Δ and with the anticrossing gap Δ_0 as a parameter.

To ensure that the greatest energy difference between electrons in subband $|2\rangle$ and $|1\rangle$ is below the LO phonon energy of $\hbar\omega_{LO} = 36$ meV, we have chosen our frequency to be about 4 THz, which corresponds to 16 meV intersubband spacing. In this way, we can safely populate the second subband up to $E_f - E_2 = 15$ meV (corresponding to a $5 \times 10^{11}/\text{cm}^2$ carrier density) without opening up the fast LO-phonon emission channel. Given $\Delta = 15$ meV, and if we choose Δ_0 to be 4.2 meV, Fig. 4 shows an oscillator strength close to 0.20, which is an acceptable value. The contour plots in Fig. 4 indicate that a barrier with approximately 25% Al concentration and a width of 24 Å will provide the desired Δ_0 . These material parameters can be controlled in a MBE growth process.

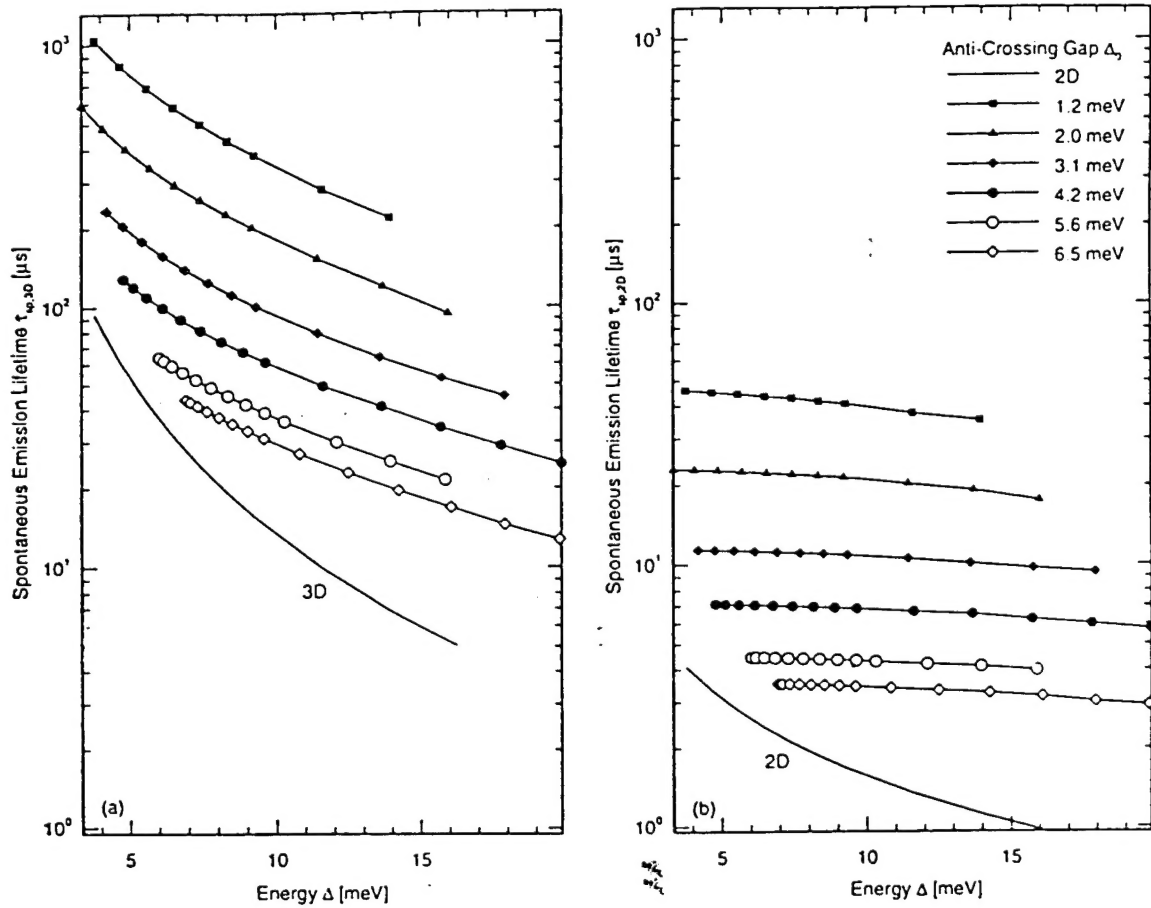


Figure 5. Spontaneous emission lifetimes for a 3D and 2D optical mode density for interwell (expressed as symbols) and intrawell (solid lines) transitions as a function of emission frequency and with Δ_0 as a parameter.

From the oscillator strength, it is straightforward to calculate the intersubband spontaneous radiative lifetime $\tau_{\text{spon}} = \frac{4 \epsilon L c^2 m^*}{e^2 \omega} \frac{1}{f_{12}}$, which determines the gain of the lasing media. Here we assume the radiation is confined between two parallel plasma walls with a separation of L . Assume $L = 3 \mu\text{m}$, τ_{spon} is plotted in Fig. 5 as a function of the energy splitting with Δ_0 as a parameter. In comparison, the radiative lifetime of a Hertzian dipole emitting in 2D is also plotted in Fig. 5, which shows a $1/\omega$ dependence (in contrast with $1/\omega^2$ dependence of a 3D dipole). The radiative lifetime τ_{spon} is almost independent of frequency because of the $1/\omega$ dependence of the oscillator strength (see Eq. (4)). For $\Delta_0 = 4.2 \text{ meV}$, this lifetime is approximately $6 \mu\text{s}$.

The gain of a medium with an inverted population Δn can be calculated from the well-known Einstein relation between spontaneous and stimulated transition rates, and is given by,

$$g(\lambda) = \frac{t_{\text{ac}}}{t_{\text{tot}}} \frac{\Delta n}{t_{\text{ac}}} \frac{\lambda^2}{4\pi\epsilon_r\tau_{\text{spon}}} \frac{T_2}{1 + (\omega - \omega_0)^2 T_2^2}, \quad (5)$$

where t_{ac} is the thickness of the active region with an inverted population, t_{tot} is the distance of photon confinement, $\omega_0 = (E_2 - E_1)/\hbar$ is the angular frequency at resonance, πT_2 is the inverse of the full linewidth of the spontaneous emission,¹⁷ and ϵ_r is the relative dielectric constant of the quantum well material. At the lasing threshold, the gain equals the total loss, which is mainly due to free-carrier absorptions in the lossy plasma walls.⁵ This loss has been calculated before and is given by,

$$\alpha = \frac{S_x}{t_{\text{tot}} S_z} \approx \frac{1}{\omega_p \tau} \frac{1}{t_{\text{tot}}}, \quad (6)$$

where S_z and S_x are the z - (along the growth direction) and x -component of the Poynting vector, respectively; ω_p is the plasma frequency, and τ is the scattering time in the plasma. Equating Eqs. (5) and (6), we obtained the lasing threshold density of population inversion, which is plotted in Fig. 6 as a function of emission frequency for two different doping levels in the plasma region. Again, the anti-crossing gap is a parameter in these calculations. Clearly, there is some benefit in using heavily doped plasmas, whose shorter penetration depths (corresponding to tighter mode confinements) more than compensate for the shorter scattering time τ at a higher doping level. The approximate $\omega^{1/2}$ increase of the threshold density is due to the $\omega^{1/2}$ increase of the plasma loss, which is analogous to the surface resistance of metals.

If we use DQW structures with a $\Delta_0 = 4.2 \text{ meV}$ and a doping concentration of $2 \times 10^{18}/\text{cm}^3$ in the plasma regions, the threshold density will be approximately $10^{13}/\text{cm}^2$. If all these electrons are placed in a single DQW device, the Fermi energy will be approximately 30 meV , which will allow fast LO-phonon scattering to occur. Furthermore, the electron-electron scattering time will be shorter than 1

ps. These two extremely fast relaxation processes will make the required inverted population density impossible to achieve. However, if we use many identical DQW modules to spread out the required inverted population, Δn will be much less than $10^{13}/\text{cm}^2$ in each of them. Consequently, the LO-phonon emission process can be avoided and the electron-electron scattering will be substantially reduced.

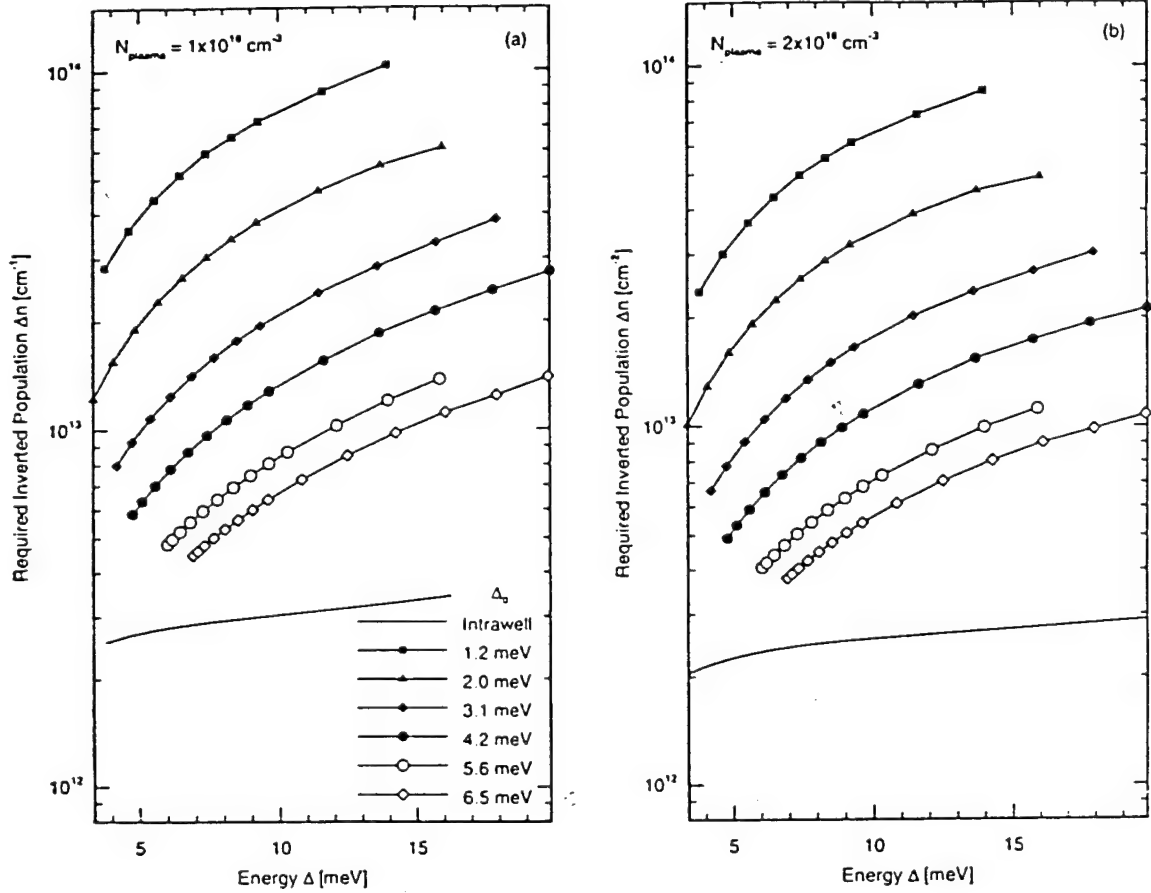


Figure 6. Threshold inverted population density required to overcome plasma confinement losses for two plasma concentrations: $1 \times 10^{18} \text{ cm}^{-3}$ (a) and $2 \times 10^{18} \text{ cm}^{-3}$ (b). For these calculations, the linewidth $1/\pi T_2$ is taken to be 20 cm^{-1} from Ref. [10].

III.2 Scattering and lasing threshold current density

The lasing threshold current density is simply given by

$$J_{\text{th}} = e(\Delta n_{\text{th}}/N) / \tau_{\text{tot}} , \quad (7)$$

where N is the number of DQW structures, and $1/\tau_{\text{tot}} = 1/\tau_{\text{ac}} + 1/\tau_{\text{LO}} + 1/\tau_{\text{e-e}}$ is the total relaxation rate. (We ignore the extremely slow τ_{spon} radiative relaxation here.) In the current project, we have made major efforts to calculate the rates of all nonradiative relaxation processes.¹⁴ We summarize the results in the following. Fig. 7 shows τ_{LO} as a function of the radiation frequency, assuming the electrons in the second subband have sufficient kinetic energy to emit an LO phonon in the case of $E_2 - E_1 < \hbar\omega_{\text{LO}}$. For $\Delta_0 = 4.2$ meV, $\tau_{\text{LO}} \sim 1$ ps for the frequency range of interest. This extremely fast relaxation makes the radiation efficiency low ($\sim 10^{-7}$) and the threshold current density prohibitively high. Thus, this channel should be avoided in any design considerations.

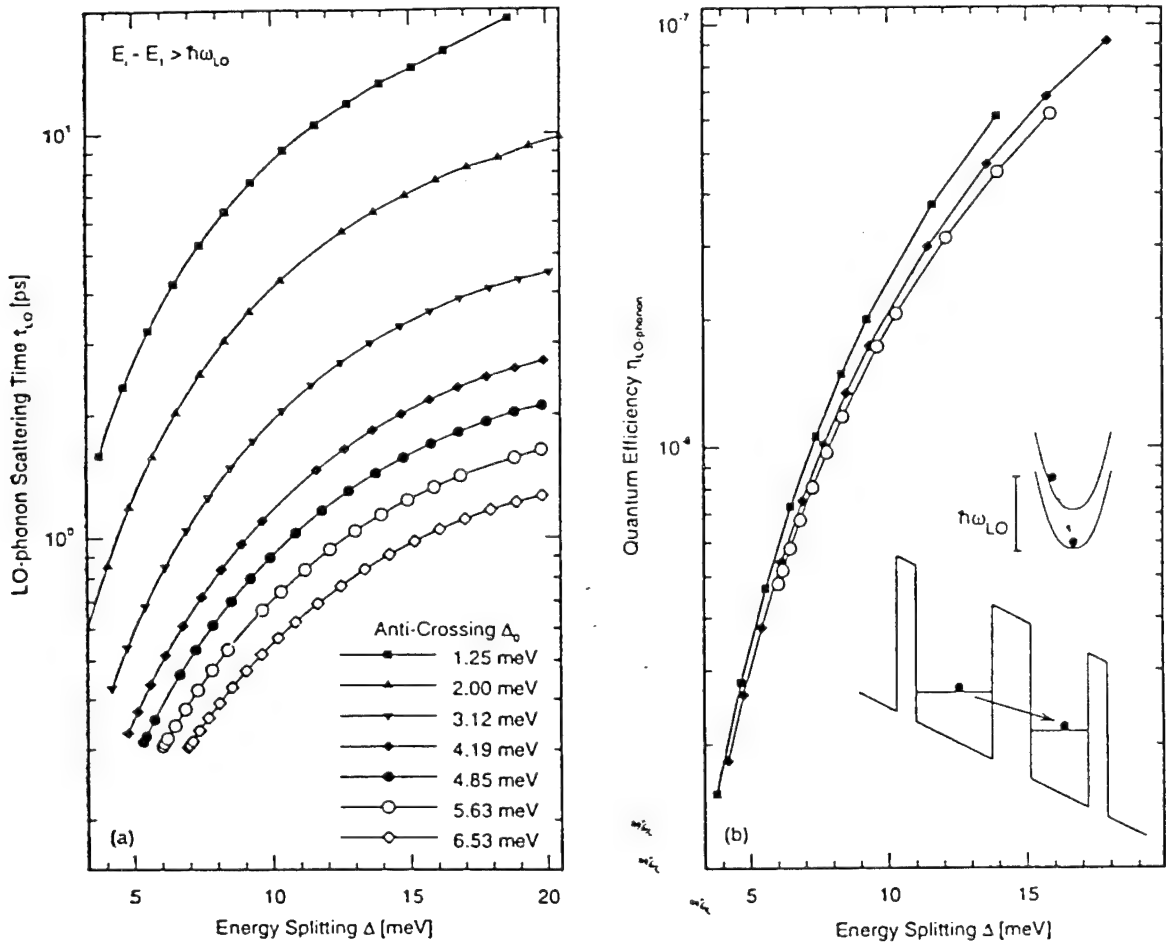


Figure 7. The GaAs-like LO-phonon scattering time τ_{LO} for a DQW structure as a function of subband spacing Δ and at different anticrossing gaps Δ_0 . The plot on the right is the radiative efficiency $\tau_{\text{LO}}/\tau_{\text{spon}}$ as a function of Δ .

Acoustic-phonon scattering is a much slower process because of the absence of singularities in the density of phonon states. Fig. 8 plots τ_{ac} as a function of frequency. Again, for $\Delta_0 = 4.2$ meV, $\tau_{ac} \sim 1$ ns. This process is sufficiently slow so that it will not require a demanding current density to reach the threshold.

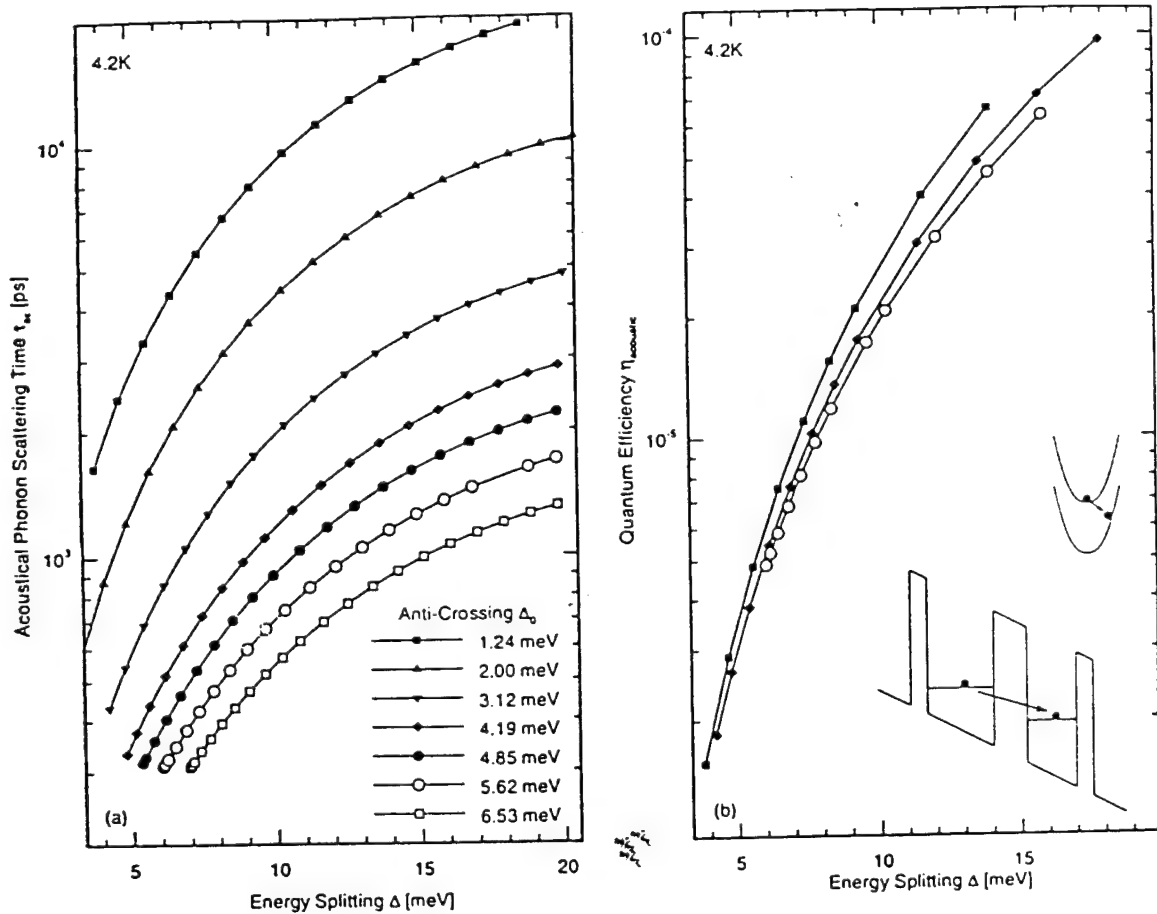


Figure 8. The acoustic-phonon scattering time τ_{ac} as a function of Δ with Δ_0 as a parameter. The plot on the right is the radiative efficiency τ_{ac}/τ_{spon} due to acoustic-phonon scattering.

Electron-electron scattering, which has been largely ignored in most of the previous work, was found to be the dominant nonradiative relaxation process in this project. Although e-e scattering is an elastic process, as far as the total energy of the two electrons is concerned, it can result in a large change of moment for each electron. Therefore, two electrons can scatter each other from the second subband to the first one, gaining a greater transverse (in-plane) momentum at the expense of longitudinal energies. These electrons will later emit phonons to lower their energies to the bottom of the first subband. As far as the radiation property is concerned, this scattering is equivalent to other nonradiative processes, such as acoustic-phonon and LO-phonon emissions, which are inelastic processes. The estimate of the e-e scattering rate is by no means trivial and some calculations remain controversial.¹⁴ Using the simplest Hartree formalism and ignoring the exchange interaction, we estimate the e-e scattering time to be approximately 30 ps for $\Delta_0 = 4.2$ meV and $\Delta = 10$ meV, for a modest carrier concentration of $1.4 \times 10^{11}/\text{cm}^2$.¹⁴ Clearly, e-e scattering is the dominant nonradiative relaxation process in the frequency range of interest.

For the required threshold density of $\Delta n_{\text{th}} \approx 10^{13}/\text{cm}^2$, if we use 70 DQW modules to reduce Δn to $1.4 \times 10^{11}/\text{cm}^2$ for each one, the lasing threshold current density from Eq. (7) will be approximately 750 A/cm². This is feasible, provided the property of these DQWs is sufficiently uniform to evenly spread out the inverted population.

III.3 Magnetic suppression of nonradiative intersubband scattering

Clearly, if we were able to reduce the nonradiative intersubband scattering rate, especially the LO-phonon and electron-electron scattering, we could reduce the lasing threshold current density J_{th} significantly; or to keep J_{th} constant, we could increase the inverted population density significantly, and therefore using fewer DQW modules and still have sufficient lasing gain. The nonradiative relaxation processes are so fast because the subbands in a quantum well have continuum states for all the possible transverse momentum values (perpendicular to the growth direction), instead of discrete energy levels. Thus, the conservation of energy and transverse momentum can be simultaneously satisfied for these processes. In a quantum dot with a zero-dimensional density of states, these processes will be significantly suppressed, since the LO-phonon process will be prohibited if the intersubband spacing is different from $\hbar\omega_{\text{LO}}$. Electron-electron scattering will also be suppressed, if the lower and upper subbands have different spacings, as illustrated in Fig. 9. In addition, the acoustic-phonon process will be reduced, because the number of available phonon modes is significantly reduced. However, a quantum dot contains few electrons, thus it will not generate much radiation power. A quantum-dot array will inevitably introduce inhomogeneous broadening. In

addition, an electric contact to such arrays will be difficult, thus making electric pumping a less feasible approach.

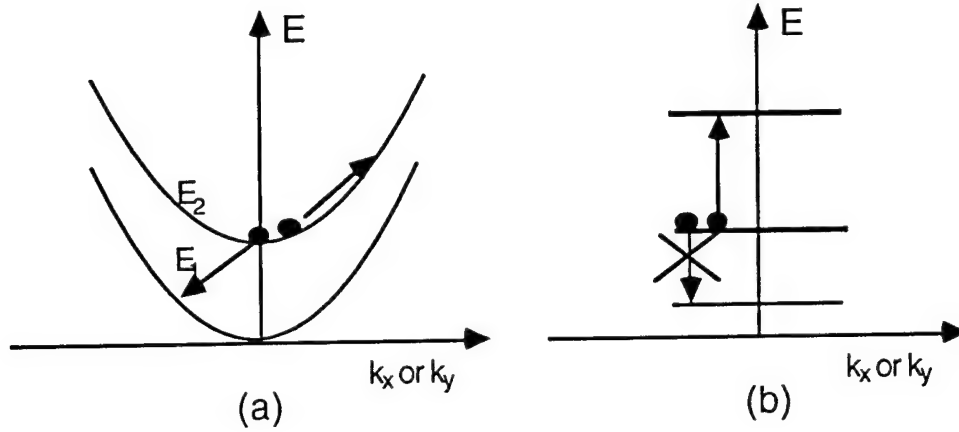


Figure 9. (a) Electron-electron intersubband scattering in a quantum well that simultaneously satisfies the energy and momentum conservation. (b) Suppression of the e-e scattering in a zero-dimensional system.

Similar to the concept employed to confine plasmas in a tokamak, several groups have proposed the use of magnetic fields to reduce the dimensionality of the electron system in order to suppress nonradiative relaxation processes.^{12,13} Under a strong field along the growth direction, the transverse motion of electrons will be confined in cyclotron orbits and their energy spectrum will be quantized at Landau levels. This magnetic field-induced transverse confinement, along with the longitudinal confinement provided by the quantum-well structures, will effectively reduce the dimensionality of the electron system to that of a zero-dimensional system, similar to that of quantum-dot systems. Consequently, the detrimental nonradiative relaxation processes will be significantly reduced. In this scheme, the applied longitudinal magnetic field will not affect transport in that direction or the dipole moment associated with the transition between two subbands. Therefore, the field will not have any adverse effect on the radiative process, and will substantially increase the radiation efficiency $\eta = \tau_{\text{nonrd}}/\tau_{\text{spon}}$.

In the current project, we have designed and fabricated appropriate MQW structures in which the current is limited by relaxation between two subbands, which is mostly nonradiative below the lasing threshold. Under a longitudinal magnetic field, this relaxation process and the current will be reduced. This will provide definitive evidence for the predicted magnetic suppression. Our preliminary measurements have yielded, at best, ambiguous results to support this mechanism.¹⁸ Other groups

pursuing this goal have experienced similar results.¹⁹ We speculate that the failure to observe the magnetic suppression is due to broadened Landau levels that resulted from impurity and interface scattering. These broadened levels provide the states for scattering which simultaneously satisfy the energy and momentum conservations. We intend to improve this measurement by using better MBE samples and stronger magnetic fields (previous work was conducted up to 15 Tesla), at which the Landau gap is opened up faster (scaled linearly with H) than the level broadening (scaled as $H^{1/2}$ [13]). This will reduce the number of states for scattering to occur. At MIT, we have the benefit of the Francis Bitter National Magnet Laboratory (FBNML), which has the high magnetic fields required for this investigation.

It will also be interesting to study the far-infrared emission properties of these DQW devices under a strong longitudinal magnetic field. If magnetic suppression occurs and does not affect the dipole intersubband transitions, the emission linewidth should be narrowed, due to reduced scattering. For the same reason, the intensity at the peak frequency of the emission spectrum should be increased, because more photons will be emitted at the same frequency. If established experimentally, this effect will be a beautiful example of magnetic field-induced reduced dimensionality, which will play an important role in device applications.

III.4 Magnetotunneling spectroscopy

Motivated by the magnetic suppression effect, we have performed extensive tunneling studies of DQWs and TQWs (triple quantum wells) in strong magnetic fields with both a longitudinal and transverse component. This study, called *magnetotunneling spectroscopy*, is a very powerful spectroscopic tool to measure the subband levels and in-plane energy-momentum dispersion (crucial information for any intersubband devices) with much greater accuracy than a dc tunneling study alone would yield.

At far-infrared frequencies of several THz, the corresponding intersubband spacing is only on the order of 10 meV (1 THz = 4 meV). For such a narrow intersubband spacing, the dc tunneling I-V characteristic measurement usually exhibits many rich features that will be difficult to unambiguously identify. Therefore, it will be difficult to determine the relative subband positions from the dc tunneling I-V curves alone. The magnetotunneling spectroscopy tool developed in this work can solve this problem easily.²⁰ The current at a fixed bias voltage of MQW structures exhibits an oscillatory dependence on the longitudinal magnetic field. This magneto-oscillation is periodic with the inverse of the magnetic field, as shown in Fig. 10, and is reminiscent of de Haas-Shubnikov (dHS) oscillations. Similar to using the dHS effect to measure Fermi energies, we can measure the intersubband spacing from the oscillation period with sub-meV accuracy [20].

The physical origin of this magneto-oscillation is scattering-mediated inter-Landau-level tunneling. Suppose the energy in the first well is $E_1 + (n_1 + 1/2)\hbar eB/m^*$, and the energy in the second well is $E_2 + (n_2 + 1/2)\hbar eB/m^*$, where E_1 and E_2 are the energies of the subbands in the first and second well. In the absence of LO-phonon emissions, energy conservation requires that the two energies be equal. Thus, $(n_2 - n_1)\hbar eB/m^* = E_1 - E_2$, or $1/B = (n_2 - n_1)\hbar e/m^*(E_1 - E_2)$. This implies that whenever $1/B$ is an integer times the inverse of a characteristic field $1/B_0 = \hbar e/m^*(E_1 - E_2)$, the energy conservation is satisfied and the tunneling current will be enhanced. This gives the oscillatory behavior of the tunneling current as a function of $1/B$, as shown in Fig. 10, whose Fourier transform will have a peak centered at the characteristic field B_0 .

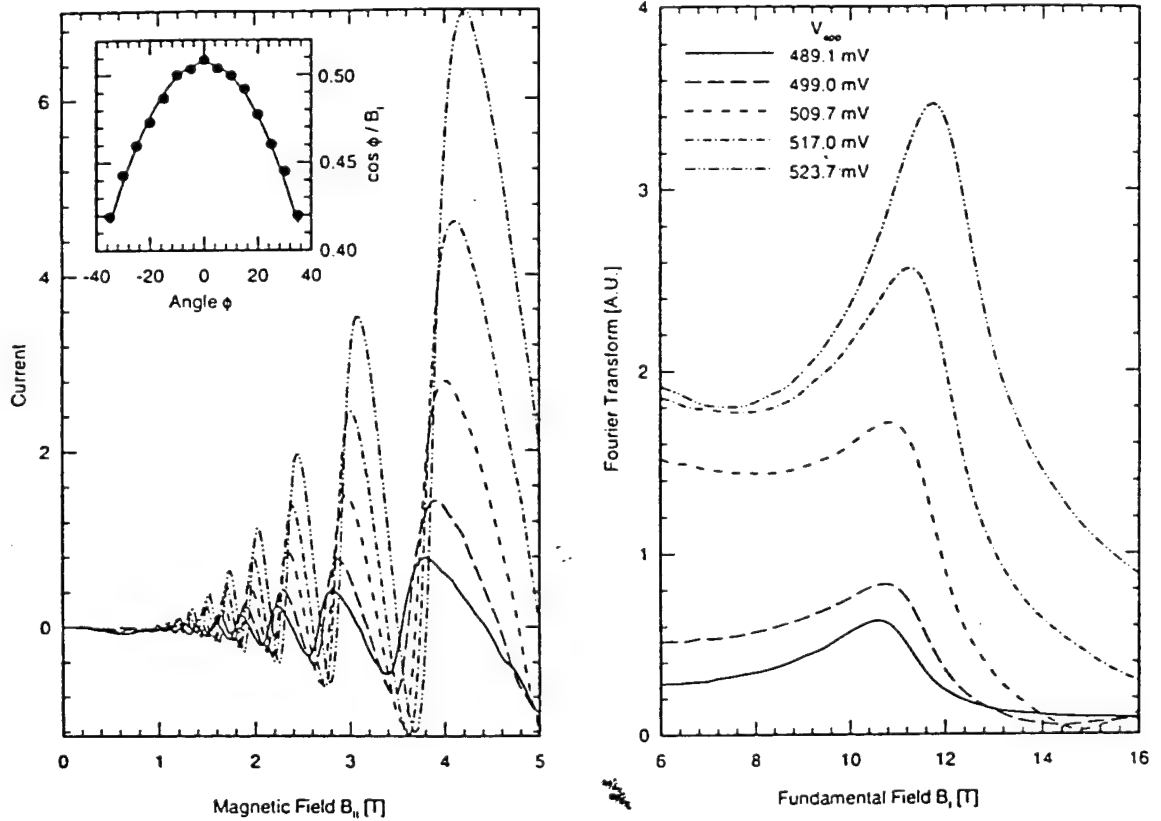


Figure 10. Magnetotunneling oscillations (left) and their Fourier transform (right) in the current of a DQW device with a bias voltage from 489 mV to 524 mV. The inset on the left shows the frequency of the magneto-oscillations as a function of the angle between the magnetic field and current flow ϕ . The $\cos \phi$ dependence is an indication that the magneto-oscillation is due to 2D-2D tunneling between two wells.

Since the energy difference between the two subbands is related to B_0 through $E_1 - E_2 = \hbar e B_0 / m^*$, magnetotunneling spectroscopy provides us with a very accurate method to measure the relative positions of the subbands. Fig. 11 shows the subband energy levels as

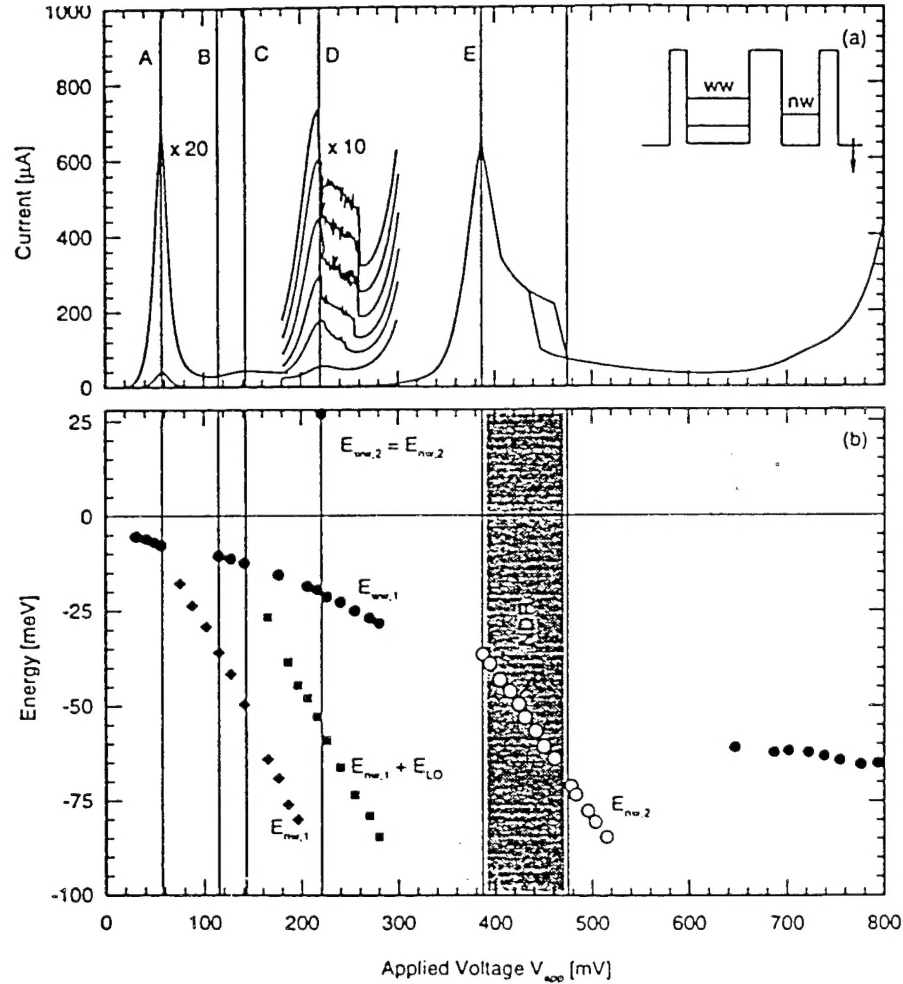


Figure 11. I-V characteristic (a) and the subband energies (b) as functions of the bias voltage at 4.2 K. The quasi-Fermi level in the emitter well is used as the energy reference (i.e. $E_{\text{FE}} = 0$). The open-circle data in the negative dynamic region (NDR) was obtained by applying an in-plane field to broaden the resonance peak.

functions of bias voltage for a DQW device. These measured energy levels are within 5% from the designed values, which is remarkable considering the relatively small energy scales (~ 10 meV) for far-

infrared applications. This accurate determination of subband energy levels is crucial to successfully develop far-infrared sources with specific frequencies.

Under a transverse or in-plane magnetic field (with the field perpendicular to the current-flow direction), as well as a longitudinal one, electrons will acquire momentum in the transverse direction while traversing the MQW structures. Thus, the conservation of transverse momentum is no longer valid. Consequently, the applied transverse field broadens the resonant peaks in the tunneling I-V characteristics, and shifts the position of the resonances to higher bias voltage, as shown in Fig. 12. Using this method, we can perform spectroscopy in the I-V curve region, where it has a negative dynamic resistance (NDR) that otherwise would be inaccessible, due to the instability associated with the NDR.¹⁸ This information is crucial for laser operation, since the NDR region corresponds to the initial state with a higher energy than the final state, which is the normal operating condition for lasers.

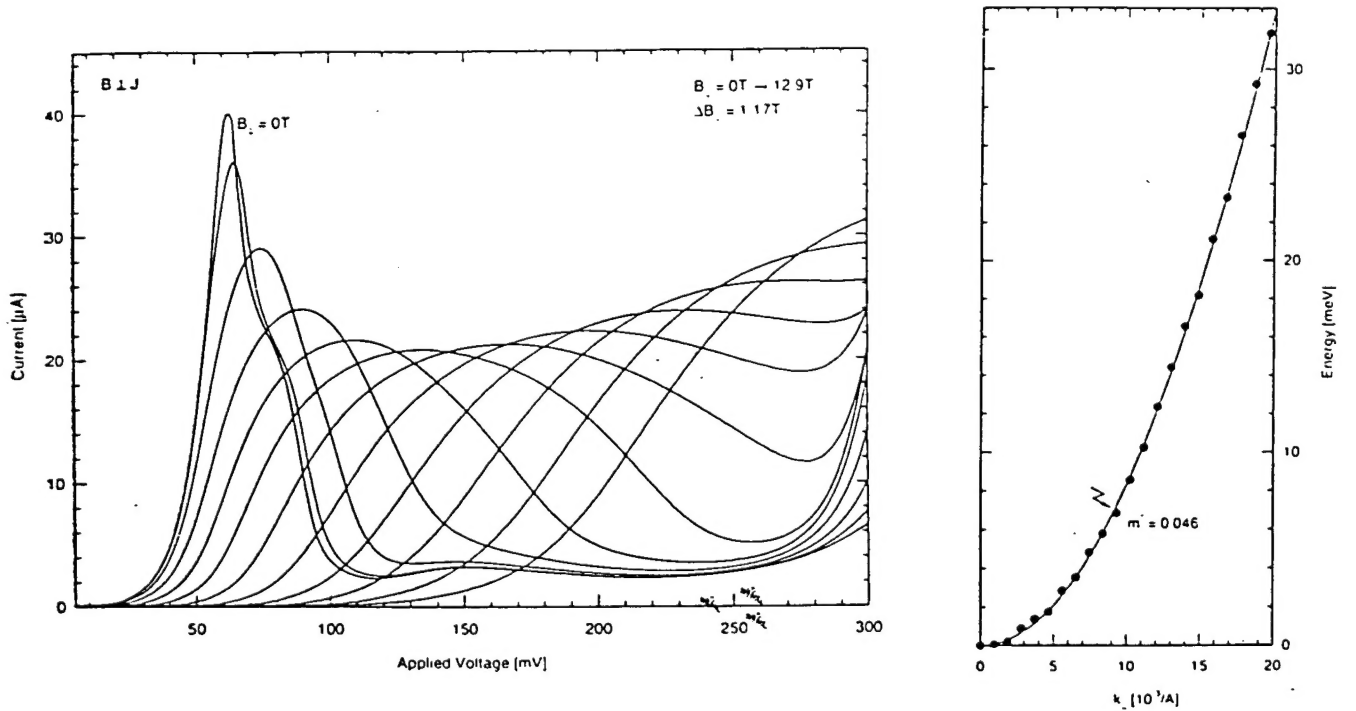


Figure 12. Left plot: I-V tunneling characteristics near resonance of an InGaAs/InAlAs DQW device with an in-plane field varying from 0 T to 12.9 T in steps of 1.17 T. Right plot: In-plane energy-momentum dispersion relation whose curvature gives the effective mass m^* , which is very close to the effective mass of bulk InGaAs materials.

In addition, by studying the shift of the current peak position as a function of the transverse field, we can accurately measure the in-plane energy-momentum dispersion relation, as shown in Fig. 12, which is another piece of useful information for the MQW structures [18].

III.5 List of participating scientific personnel

- | | | |
|---------------|-----|----------------------------------------------------------------------------------------------------------------------------------------------------------------------------------------------|
| Qing Hu | --- | Principal investigator, Associate Professor of Electrical Engineering, |
| C. G. Fonstad | --- | co-principal investigator, Professor of Electrical Engineering, |
| J. H. Smet | --- | formerly graduate research assistant, Ph. D. awarded in October, 1994, title:
"Intrawell and Interwell Intersubband Transitions in Single and Multiple
Quantum Well Heterostructures," |
| B. Xu | --- | graduate research assistant. |

REFERENCES

1. R. F. Kazarinov and R. A. Suris, Sov. Phys. Semicond. **5**, 707 (1971).
2. P.F. Yuh and K.L. Wang, Appl. Phys. Lett. **51**, 1404 (1987).
3. H.C. Liu, J. Appl. Phys. **63**, 2856 (1988).
4. S.I. Borenstain and J. Katz, Appl. Phys. Lett. **55**, 654 (1989).
5. Q. Hu and S. Feng, Appl. Phys. Lett. **59**, 2923 (1991).
6. A. Kastalsky, V. J. Goldman, and J. H. Abeles, Appl. Phys. Lett. **59**, 2636 (1991).
7. L.C. West and S.J. Eglash, Appl. Phys. Lett. **46**, 1156 (1985).
8. Y.J. Mii, K.L. Wang, R.P.G. Karunasiri, and P.F. Yuh, Appl. Phys. Lett. **56**, 1046 (1990).
9. M. Helm, E. Colas, P. England, F. DeRosa, and S.J. Allen, Jr., Appl. Phys. Lett. **53**, 1714 (1988).
10. M. Helm, P. England, E. Colas, F. DeRosa, and S.J. Allen, Jr., Phys. Rev. Lett. **63**, 74 (1989).
11. J. Faist, F. Capasso, D. L. Sivco, C. Sirtori, A. L. Hutchinson, and A. Y. Cho, Science **264**, 477, (1994); J. Faist, F. Capasso, D. L. Sivco, C. Sirtori, A. L. Hutchinson, and A. Y. Cho, Electron Letters, **30**, 865 (1994).
12. A. Kastalsky and A. L. Efros, J. Appl. Phys. **69**, 841 (1991)

13. A. Blank and S. Feng, J. Appl. Phys. **74**, 4795 (1993).
14. J. H. Smet, C. G. Fonstad, and Q. Hu, submitted to J. Appl. Phys. (1995).
15. L. D. Landau and M. D. Lifshitz, "Quantum Mechanics (Non-relativistic theory)", 3rd ed., London, Pergamon Press (1977).
16. S. Luryi, IEEE J. QE-**27**, 54 (1991).
17. A. Yariv, *Quantum Electronics*, Chapters 8 and 9, 2nd ed. John Wiley & Sons, New York (1989).
18. J. H. Smet, C. G. Fonstad, and Q. Hu, to be submitted to Phys. Rev. **B**, (1995).
19. K. von Klitzing, private communication through J. H. Smet (1994).
20. J. H. Smet, C. G. Fonstad, and Q. Hu, Appl. Phys. Lett. **63**, 2225 (1993).
21. A. N. Korotkov, D. V. Averin, and K. K. Likharev, Appl. Phys. Lett. **65**, 1865 (1994).